Journal of Metals, Materials and Minerals, 36(3), e2654, 2026

Performance of the heat affected zone of 9% Ni steel narrow gap joint performed by the GMAW process with rotating electrode

Jorge Carlos Ferreira JORGE[1,*], Jeferson Frederico Monteiro COSTA[1], Matheus Campolina MENDES[1], Luís Felipe Guimarães de SOUZA[1], Hiron Akira Yamada MAGALHÃES[1], and Leonardo Sales ARAÚJO[2]

[1] *Centro Federal de Educação Tecnológica Celso Suckow da Fonseca (CEFET-RJ), Avenida Maracanã 229, Rio de Janeiro, 20271-110, Brazil*
[2] *Universidade Federal do Rio de Janeiro, Rio de Janeiro, 20271-110, Brazil*

***Corresponding author e-mail**: jorgecfjorge@gmail.com

Received date:
11 February 2026
Revised date:
30 April 2026
Accepted date:
4 June 2026

Keywords:
GMAW-RE process;
9% Ni steel;
Mechanical properties;
Microstructure;
Productivity

Abstract

This work investigates the mechanical properties and microstructural evolution of the heat-affected zone of 9% Ni steel narrow-gap welded joints produced by the GMAW process with a rotating electrode, since no literature on this subject is available. This process is an innovation of the GMAW process, which permits narrow gap welding because the circular motion of the electrode overcomes the main issue of the sidewall's lack of fusion observed in the conventional process. However, the rotation movement of the electric arc imposes a higher peak temperature at the heat affected zone, which can negatively affect the mechanical properties. The joints were welded in the flat position, preheated to 100°C, with a rotation frequency of 1500 rpm, a rotation diameter of 3 mm, and an average heat input of 2 $kJ \cdot mm^{-1}$. The results obtained in metallographic examination by electron microscopy and backscattering diffraction, and tensile and Charpy-V impact tests revealed similar behavior of the heat-affected zone compared with the base metal. Thus, it is concluded that the 9% Ni steel welded by the GMAW process with a rotating electrode can be an advantageous alternative due to its higher productivity and mechanical properties that meet the requirements for industrial applications.

1. Introduction

The consumption of liquefied natural gas (LNG) has grown significantly over the last decades and today accounts for about 15% of the total natural gas supply [1,2]. LNG is gradually replacing coal and oil, leading to a fast development of cryogenic storage tanks [3]. LNG only takes 1/600 of the volume of the gas at standard atmospheric pressure [4,5], thus improving its storage and transportation without the need for pipelines. The gas stored and transported in vessels is usually liquefied at minus 162°C and sealed in dedicated tanks [4,6]. The manufacturing of tanks for LNG requires steels that sustain their impact toughness even at the low temperatures mentioned due to the high danger potential [4]. In this respect, the 9% Ni steel is selected preferentially [4] over austenitic steels due to its lower cost, attaining the minimum impact energy of 0.75 $J \cdot mm^{-2}$ at –196°C, corresponding to 60 J on a standard Charpy impact specimen, specified for the LNG storage tanks [1]. The 9% Ni steel with tempered martensite has been widely used around the world as base metal in the manufacture of LNG tanks using plate thickness in the range from 5 mm to 35 mm [7,8] without the need for post weld heat treatment due to its excellent cryogenic properties [1,6,9] associated with acceptable price and proper workability at low temperatures [9]. According to Serindag *et al*. [1], austenitic stainless steels cost 3.7 euros$\cdot kg^{-1}$ while the price of 9% Ni steel is approximately 2.5 euros$\cdot kg^{-1}$.

Welding is an unavoidable method in the manufacturing process of LNG tanks [5,10,11]. As a consequence, the low-temperature properties of the welded joints have attracted attention [12]. Usually, shielded metal arc welding (SMAW), gas tungsten arc welding (GTAW), gas metal arc welding (GMAW), flux cored arc welding (FCAW), and submerged arc welding (SAW) processes are applied for welding LNG tanks with 60° V or double V-groove joints, depending on the thickness [1,5,8,10,12–14]. Although SMAW and SAW are the common welding processes for 9% Ni steel, the traditional SMAW welding process has low welding efficiency, and SAW has limitations in welding position [15]. Cheon *et al.* [8] stated that FCAW has emerged as a preferred method due to its advantages, such as higher deposition rate, continuous wire feed enabling long welds without interruption, positional welding, and easier slag removal.

In addition, the welding of the 9% Ni should be strictly controlled due to the poor environmental conditions in the on-site welding work of LNG tanks [11]. Zhu *et al*. [15] state that the development of a 9% Ni steel welding method with a high deposition rate, thereby reducing the number of welding passes and improving the uniformity and purity of the weld metal, is an urgent task. As filler metals, Ni-based filler materials are the most common choice for welding of LNG facilities [5,8] due to their combination of suitable mechanical properties at low temperatures, good corrosion resistance, and an expansion coefficient similar to the 9% Ni steel.

Regardless of the quality of the materials, the welding can still show various issues, such as hot cracking [6,8,13], partially diluted zones at the fusion line [3,12], martensite with a high hardness at the CGHAZ [16], and toughness deterioration for high dilution ratios [8,14].

To minimize these issues, a practical approach to achieving the desired properties is to use a reduced number of passes with a lower heat input [14]. Although some novel low-dilution welding processes have been recently employed to improve the joint efficiency, Serindag *et al*. [14] noted that reliable welding procedures with appropriate low-temperature impact toughness are still needed for 9% Ni steel

In this regard, narrow gap welding has been adopted as a good solution in various segments, such as shipbuilding and petroleum industry [7]. Also, new developments using the rotating arc have emerged as the ideal solution because the lack of sidewall and/or inter-run fusion continues to be the main issue for NGW. Besides overcoming the lack of fusion, the benefits of the rotating arc include the stirring action on the molten pool with the consequent refinement of the weld metal [7127]. The rotation movement of the electric arc leads to a broader distribution of the heat, thus resulting in a wider and shallower penetration profile, improved sidewall fusion, and a potential reduction in residual stress and dilution.

From the above-presented scenario, it can be inferred that this trend indicates that the GMAW process with Rotating Electrode (GMAW-RE), an innovation of the GMAW process, can be suggested as an interesting alternative, as it incorporates all the desired characteristics for performing quality NGW. The rotating movement of the electric arc forces the metallic droplets radially due to the centrifugal force, changes the temperature profile, and promotes a wider heat distribution beneficial for NGW, thus reducing the risk of the lack of sidewall fusion [18–20]. Besides the higher productivity and a cost reduction of approximately 30% [19], recent studies [18–22] have also shown that special alloy steel welded joints with suitable mechanical properties can be obtained. Regardless of the promising results obtained with other alloys, it is important to mention that the properties of the heat-affected zone (HAZ) can be compromised due to slower cooling rates imposed by the different thermal cycles generated by the GMAW-RE process, thus needing a deeper investigation into this subject. In this regard, no work addressing the effects of rotating arc on the properties of the HAZ of the 9% Ni steel welded joints is available.

This work shows innovative results involving the performance of a narrow gap welded joint performed with the GMAW-RE process to evaluate its feasibility to replace other conventional methods for welding of LNG tanks manufactured in 9% Ni steels, since a higher productivity associated with appropriate properties can be obtained.

2. Experimental

2.1 Materials

9% Ni steel plates with dimensions 200 mm × 130 mm × 7.0 mm were adopted as base metal. A 1.1 mm diameter solid wire of the class AWS A5.14 ERNiCrMo-3 was used as filler metal, and Ar 25% He with a flow rate of 25 L·min^{-1} was applied as shielding gas. Table 1 presents the composition of the base and deposited weld metal obtained by optical emission spectroscopy.

2.2 Welding

Initially, three beads on plate (BOP) using the electric parameters shown in Table 2 were deposited with rotation frequencies of 500 rpm, 1500 rpm, and 2500 rpm in order to select the most appropriate frequency. The welding parameters were obtained from a portable welding parameter monitoring system, with an acquisition rate of 5 kHz. The rotation diameter of 3 mm was based on the recommendations from previous works, which used the same joint geometry adopted in this work [18,19].

Afterward, a narrow gap welded joint (NGJ) with the geometry shown in Figure 1 was obtained with 2 welding passes using the electric parameters shown in Table 2, and the rotation frequency was 1500 rpm based on the results obtained on BOP tests. A Miller welding power source model Millermatic 350P with pulsed current (synergic mode) coupled a special torch with 350A and control system BINZEL ABIMIG Spin Arc was used. The welding parameters were acquired using a welding process monitoring system (Figure 2e) that executes the acquisition of welding current, voltage, time, and power. Figure 2 shows the equipment, assembling and visual aspect of the NGJ after welding.

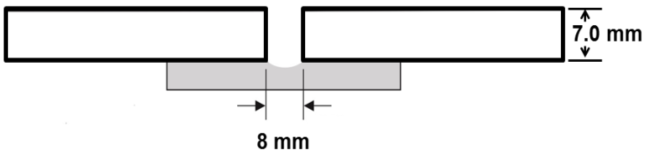

Figue 1. Weld joint geometry.

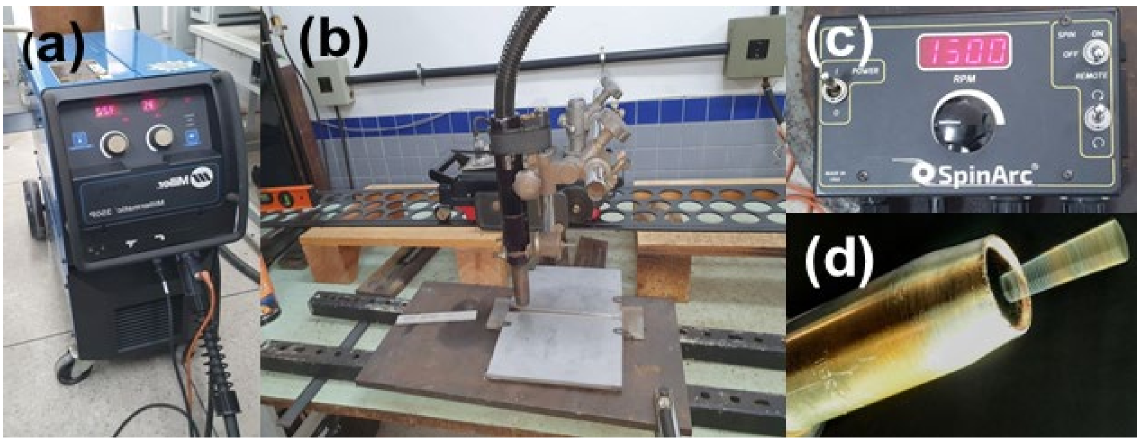

Figure 2. Apparatus for welding and visual aspect of the narrow gap joint. (a) welding machine; (b) assembling for welding; (c) frequency controller; (d) welding torch showing the rotating wire.

Table 1. Chemical composition of the materials obtained by optical emission spectroscopy.

Material	**C**	**Mn**	**Si**	**Cr**	**Mo**	**Ni**	**Cu**	**V**	**Nb**
Base metal	0.06	0.59	0.26	0.23	0.13	8.76	0.03	0.005	-
Weld metal	0.04	0.13	0.07	18.67	7.17	53.6	0.01	0.006	3.17

Table 2.Welding parameters.

Current (*) [A]	**Voltage (*) [V]**	**Welding speed [mm·s^{-1}]**	**Wire feed speed [mm·s^{-1}]**	**Heat Input (**) [kJ·mm^{-1}]**	**Deposition rate [kg·h^{-1}]**
224	33	3.3	148	1.90	3.95

(*) Mean value from acquisition data system; (**) Efficiency factor adopted was 0.85

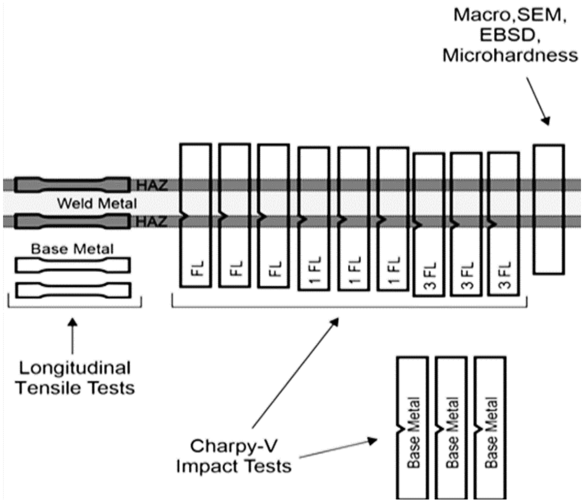

Figure 3. Schematic view of the distribution of test specimens in the narrow gap joint.

2.3 Metallographic examination

Macro and micrographic examinations were carried out in samples removed from the bead on plate (BOP) and narrow gap joint (NGJ).

From BOP samples, the main geometric characteristics, penetration, thickness, and width, were measured directly by optical microscopy (OM) with the aid of the Stream Essentials software.

Besides the macrograph, the transverse sample removed from the NGJ was examined by optical microscopy (OM), scanning electron microscopy (SEM) and Electron Back Scattering Diffraction (EBSD) in regions related to heat affected zone and base metal to clarify the main microstructural characteristics.

OM microscopy was used for the BOP samples and to observe the occurrence of retained austenite in NGJ with Le Pera's etchant, while SEM images were obtained in the secondary mode to separate martensite and bainite. Phase maps obtained by the EBSD technique were also used to reveal and quantify the presence of austenite.

The EBSD maps were collected with SEM operating at 20 kV and step size of 0.3 μm, square grid of 300 μm × 300 μm, and a confidence index of 0.86. The sample was tilted at 70°, maintained at a working distance of 20 mm. Crystallographic maps were generated using the HKL Channel 5 software package. High-angle grain boundaries (HAGB, misorientation>15°) were distinguished by the misorientation between adjacent pixels. Phase maps were used to separate austenite from the other phases.

The application of these complementary techniques was necessary to clarify all microstructural characteristics influencing mechanical properties.

The samples were examined after grinding and polishing with diamond paste of 6 μm, 3 μm, 1 μm, and 0.25 μm. For EBSD, automatic polishing with 0.06 μm colloidal silica suspension was also used. The etchants applied was nital 4% for the base metal and, by electrolytic technique, with a 10% oxalic acid solution for the weld metals. Le Pera's etching was also applied to reveal retained austenite. Aqua regia was used as the etchant for macrographs.

Additional EDS analysis was performed to evaluate the compositional transition at the base metal and the weld metal interface.

The microstructural analysis was conducted using an Olympus model BX60M optical microscope (OM), and a using a in a scanning electron microscope (SEM) from Cambridge Instruments, model Cam Scan 3200LV, with an electron backscatter diffraction (EBSD) detector.

2.4 Mechanical tests

Transverse test specimens were removed at 1 mm from the joint surface at the positions shown in Figure 3 for tensile, impact Charpy-V, and microhardness tests.

Tensile tests were executed at room temperature in two longitudinal round specimens with 4 mm diameter following ASTM E8 [23], removed at the HAZ and base metal for comparison. An Instron Universal Testing Machine Model 5985 with 250 kN capacity was employed. The travel speed (crosshead travel speed) employed was 3 mm·min^{-1}. Charpy-V impact tests at –196°C temperature. Charpy-V impact tests in a Wolpert impact test machine with 300 J of energy were also conducted on sets of three sub-size specimens (5 mm × 10 mm × 55 mm) cut transverse to the weld bead. Sub-size specimens were used due to the small thickness. The notch was positioned in the thickness section at the fusion line (FL), 1 mm (1FL), and 3 mm (3FL) from the fusion line, representing the heat affected zone (HAZ), and base metal. Vickers microhardness tests were performed in an Instron-Wilson Microhardness Testing Machine Model 402 MVD with a 500 gf. load, and a dwell time of 15 s at three parallel lines corresponding to the surface, mid-thickness, and root regions of the transverse macrograph.

3. Results

3.1 Bead on Plate

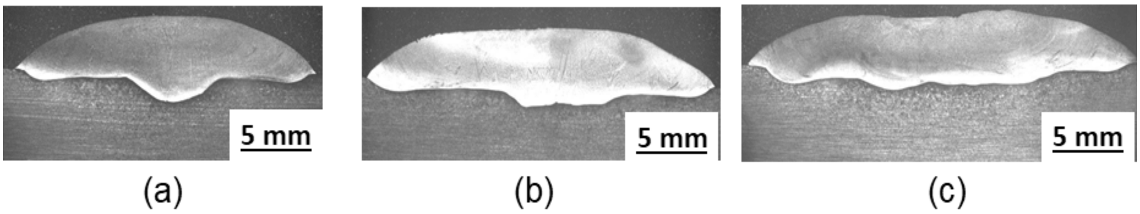

Figure 4. Macrograph of the BOP deposits after etching with aqua regia and nital 2%. (a) 500 rpm; (b) 1500 rpm; (c) 2500 rpm.

Figure 4–5 show the BOP deposits' macrograph and geometric characteristics, where no significant changes are obtained for penetration and thickness. The difference is the weld bead profile, with a tendency for the expected wider and flatter beads for higher frequencies [24].

Figure 6 shows the micrographs of the fusion line observed with low magnification by OM. The most prominent detail is the presence of a partially diluted zone (PDZ) solely for 500 rpm.

3.2 Narrow gap joint

Figure 7 shows the macrograph of the narrow gap joint (NGJ) with an adequate superficial aspect of the surface and root. The absence of defects, mainly the lack of fusion on sidewalls, is noted.

Figure 8 shows micrographs of the fusion boundary free of PDZ. Besides, EDS (Figure 8(c)) analysis confirms that the narrow transition zone (TZ) with ~20 μm observed in Figure 8(b), is composed of austenite due to the indicated basic composition (Cr_{eq}-11; Ni_{eq}-31), which is characteristic of austenite (Figure 8(d)). It is confirmed in the phase maps obtained by the EBSD technique (Figure 9).

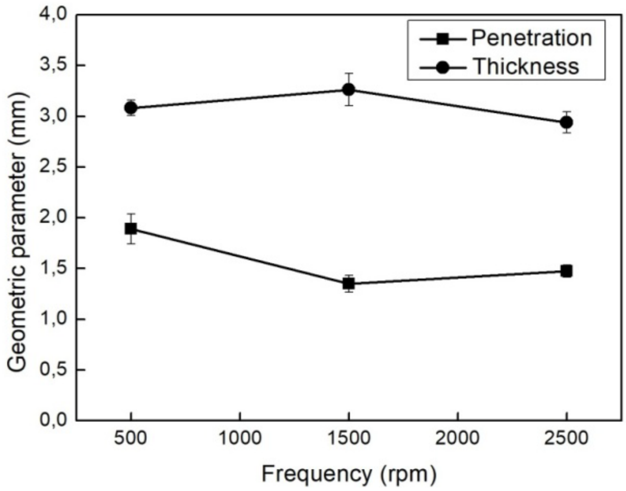

Figure 5. Geometric measurements of the BOP deposits.

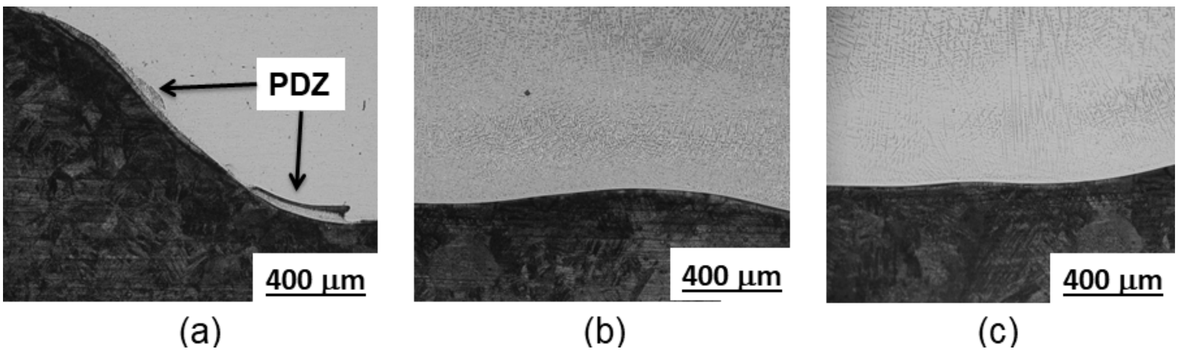

Figure 6. OM images of the fusion line showing the occurrence of PDZ for the lower frequency after etching with aqua regia and nital 4%. (a) 500 rpm; (b) 1500 rpm; and (c) 2500 rpm. Where: PDZ – Partially diluted zone.

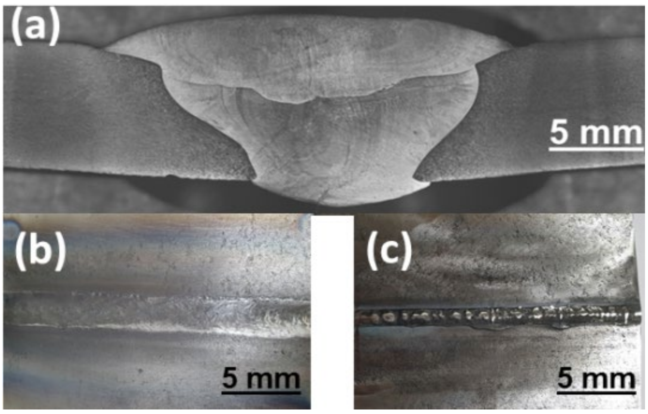

Figure 7. Details of the narrow gap joint. (a) Macrograph after etching with aqua regia; (b) visual aspect of the surface; and (c) visual aspect of the root region.

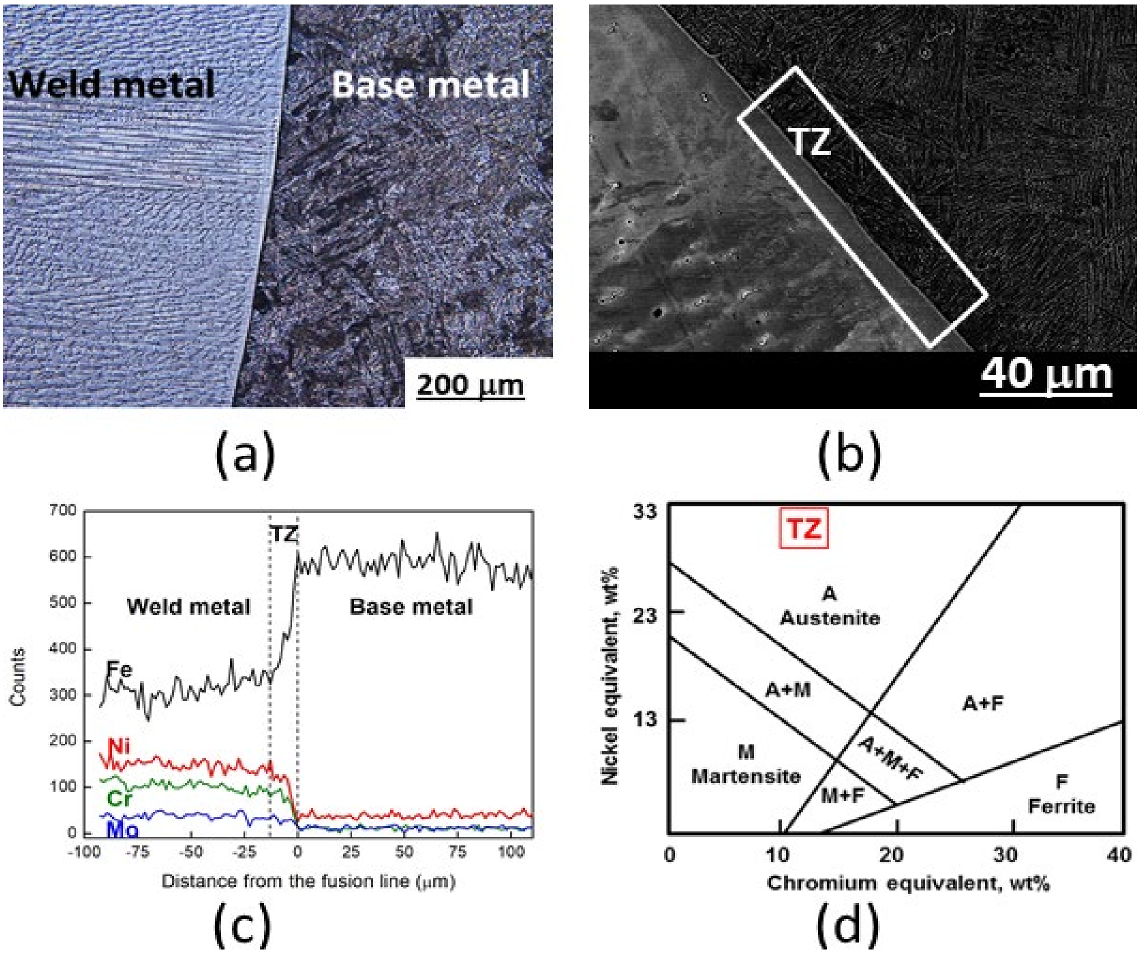

Figure 8. Details of the characteristics observed in the fusion line. (a) OM image after etching with nital 2% and oxalic acid, (b) SEM image in the backscattered mode, (c) EDS line analysis, and (d) Schaeffler diagram indicating the austenitic microstructure of the TZ.

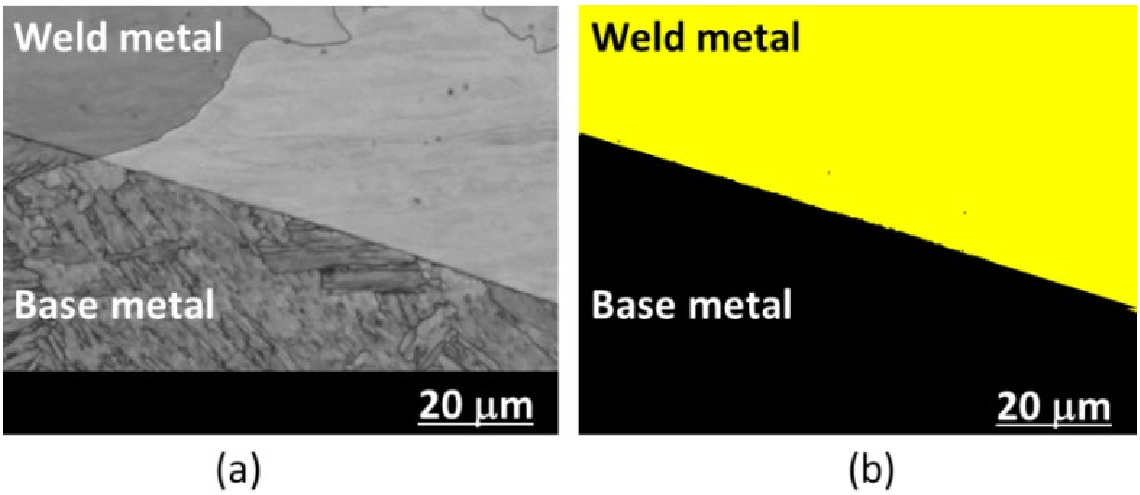

Figure 9. Band contrast map (a) and phase map (b) obtained by the EBSD technique. Austenite and martensite are represented by yellow and black colors, respectively, in the phase map.

Figure 10 shows the microstructure of the coarse grain of the HAZ (CGHAZ) along the thickness with tempered martensite (M) and bainite (B). Although the predominance of martensite, bainite, and austenite is noted for all positions, significant differences are noted at the surface of the joint, as shown in Figure 11. The base metal presents tempered martensite, austenite, and carbides, as expected, and the predominance of martensite in the banding region is revealed by Le Pera's etching (Figure 11(d)) and confirmed by the EBSD technique (Figure 11(L)). At 3 mm from the fusion line (3FL), it is observed that the peak temperature was low and no phase transformation occurred in this position. As the distance from the fusion line diminishes, a coarser microstructure is observed containing the predominance of tempered martensite (M), coalesced bainite (B), and the undesirable occurrence of fresh martensite (M_F), as shown in Figure 11(a). The formation of fresh martensite consumed a significant amount of alloying elements (C, Mn, Ni), thus limiting the fraction of austenite (Table 3). It can be responsible for the higher peak at 60° for these positions (Figure 12). Despite the lower grain size and the higher fraction of HAGB>15°, the base metal shows a lower fraction of HAGB>55° and Σ3 boundaries (Table 3).

The fractions of austenite determined by EBSD and OM using Le Pera's etchant were similar. They are in the same scatter band, although a higher dispersion is observed for shorter distances from the fusion boundary (Table 3). The values usually observed in base metals varies from 5% to 15% [25]. Although X-ray diffraction is usually the method for this task, the EBSD technique can produce equivalent results compared to X-ray [26,27]. In addition, it is essential to note that the regions analyzed in this work are very small, which could complicate the X-ray analysis.

The microhardness profile (Figure 13) follows the microstructure with the highest values observed at the CGHAZ near the fusion line, although the results are lower than those observed in other works due to the presence of bainite [5,6,8,28,29]. The results decrease with increasing distance from the fusion line, but it is important to emphasize that they are not lower than the base metal, which indicates that no softening occurred as a consequence of a higher heat flow to the HAZ. The tensile tests (Table 4) revealed equivalent results for HAZ and base metal, both meeting the requirements for 9% Ni steel [30].

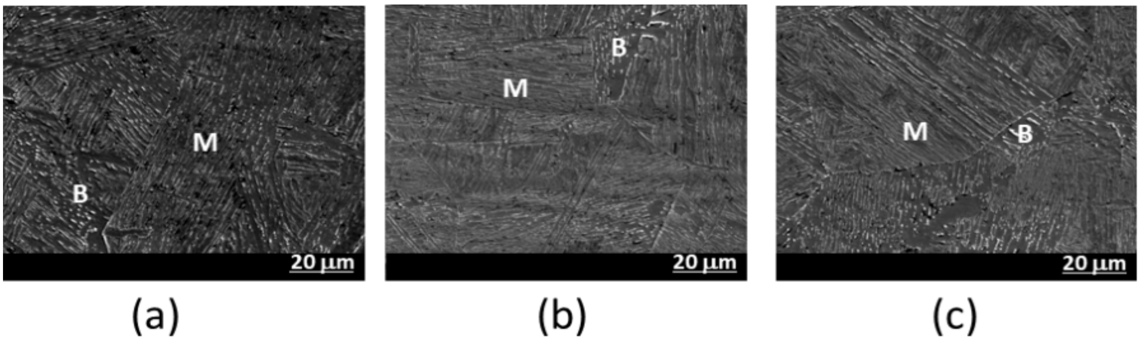

Figure 10. SEM images of the HAZ close to the fusion line showing the predominance of tempered martensite (M) and bainite (B). Etching: nital 4%.(a) Surface; (b) Mid-thickness; (c) Root.

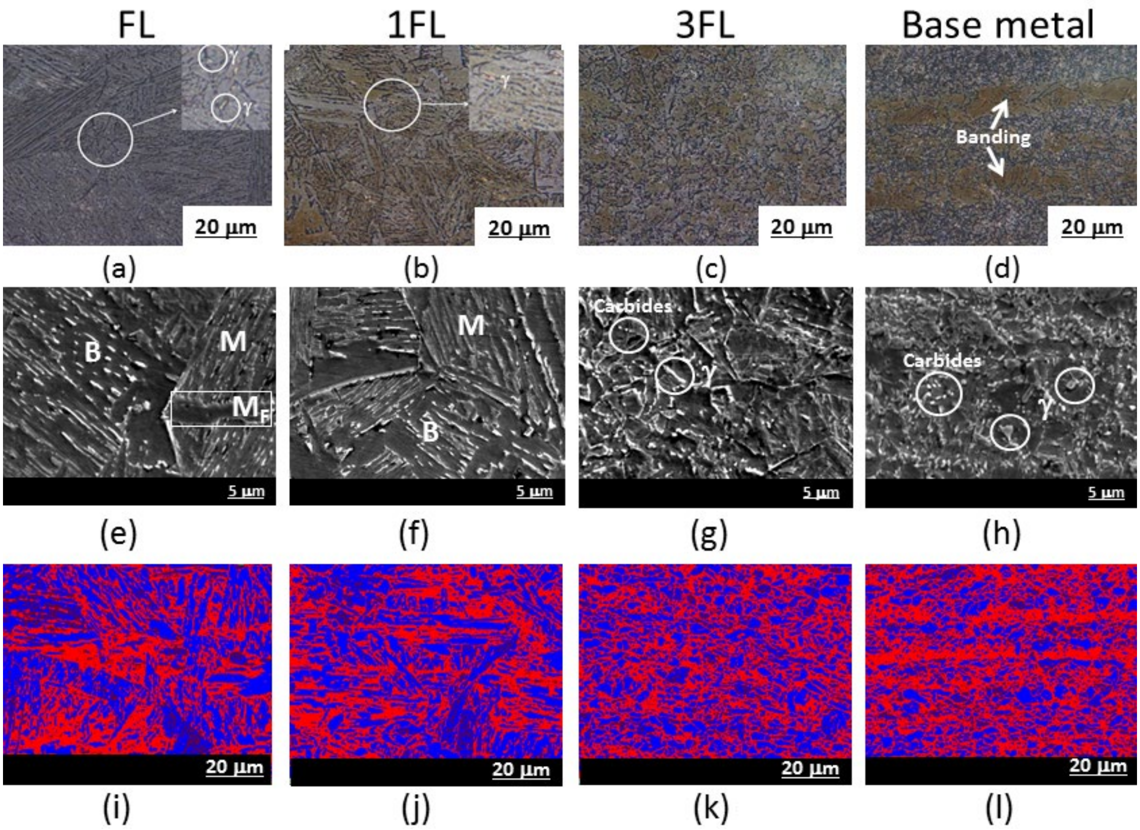

Figure 11. Microstructure of the HAZ and base metal (BM) at different distances from the fusion line (FL) at the surface. (a-d) OM micrographs after Le Pera's etching with evidence of austenite (γ); (e-h) SEM images after etching with nital 4% revealing the occurrence of martensite (M), bainite (B), and banding in the base metal; Band contrast maps from EBSD analysis with the distribution of martensite and bainite represented in red and blue color, respectively.

Table 3 Special characteristics obtained from microstructural characterization at the surface of the joint by the EBSD technique.

Position Relative frequency (%)	FL	1FL	3FL	Base metal
<15°	66 ± 1	73 ± 3	64 ± 1	61 ± 1
>15°	34 ± 1	29 ± 3	36 ± 1	39 ± 1
>55°	20 ± 4	21 ± 3	13 ± 1	11 ± 1
□3 (%)	14.8 ± 1.1	9.6 ± 1.1	4.7 ± 0.2	4.0 ± 0.1
Austenite (%)	4.8 ± 2.8	7.1 ± 2.5	5.7 ± 0.3	6.8 ± 0.1
Grain Size (□m)	109 ± 18	60 ± 9	11 ± 2	11 ± 2

Where: FL – Fusion line; 1FL – 1 mm from the fusion line; 3FL – 3mm from the fusion line.

Table 4. Results of tensile tests.

Type	**Position**	**YS [MPa]**	**UTS [MPa]**	**El (%)**
Longitudinal	HAZ	688 ± 7	756 ± 11	35 ± 1
Longitudinal	Base metal	707 ± 3	739 ± 1	37 ± 2
ASTM A 533 Tp1 [44]		585	690 to 825	20

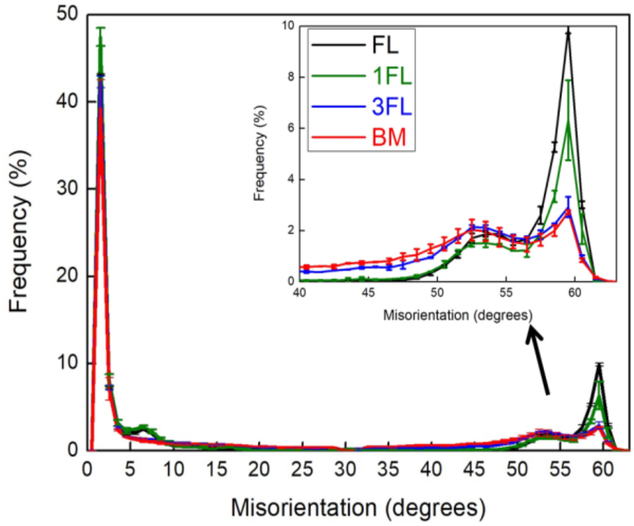

Figure 12. Misorientation profile and frequencies of high angle grain boundaries (HAGB) for the same positions observed in Figure 11.

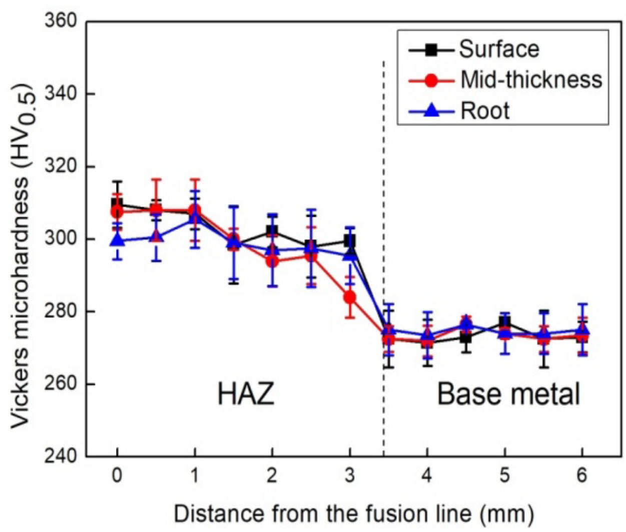

Figure 13. Results of microhardness ($HV_{0.5}$) measured at different distances from the fusion line.

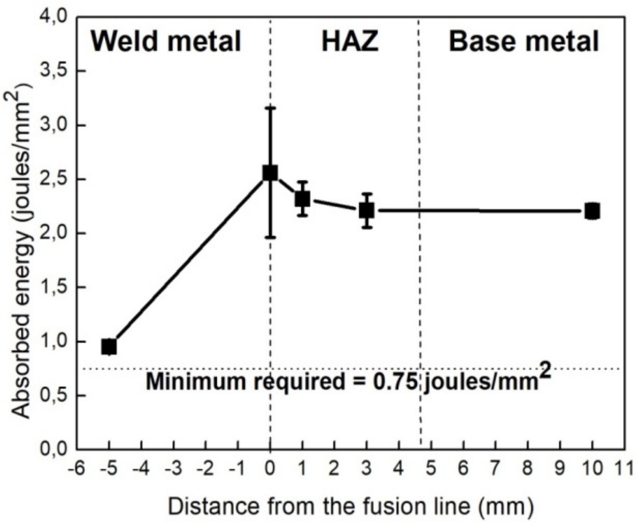

Figure 14. Results of Charpy-V impact tests performed at –196°C

Figure 14 shows the results of the impact tests performed at –196°C, where it is worth noting that the values of the HAZ are equivalent to the base metal and, significantly higher than the minimum value of 0.75 J·mm^{-2} required for LNG tanks. The high standard deviation observed at the fusion line can be due to the significant variation of the path of the fusion line along the thickness, as observed in the macrograph shown in Figure 7(a);

4. Discussion

The optimization of productivity by using narrow gap welding is widely used in industry. However, the usual lack of sidewall fusion still renders various procedures inadequate due to defects. Thus, the implementation of the GMAW-RE process has been employed as an efficient solution to overcome this issue [18], as observed in this work.

Besides the productivity advantages gained by performing a narrow gap joint, this work showed promising results that encourage further research involving the GMAW-RE process. The main finding is that the welded joint is free of sidewall lack of fusion with a HAZ that attains all technical requirements for industry application. This is unique work in revealing this scenario in the available literature. In addition, the following novelties must be emphasized since they show a superior performance compared with other conventional processes used in the manufacturing of LNG tanks [3,8,12,14,34,35].

1) Fusion boundary without the occurrence of martensite.

An important concern is the interface with the weld metal since this region usually presents complex behavior due to the high dilution ratio and can form martensite with high hardness and low toughness [12], which can contribute to the failure in service [12,31–33]. According to Mu *et al*. [12], the transition zone can be the weakest part of cryogenic toughness. It is a subject often addressed in claddings, but rarely mentioned in groove joints. However, as the fusion boundary is a critical region of the welded joint, the formation of austenite is crucial to avoid the occurrence of hydrogen cracking and, consequently, to increase the quality and safety of the welded joints.

For the 9% Ni steel welded joints using Inconel 625 as the filler metal, the elevated difference in liquidus temperature between the base metal (~1500°C) and the filler metal (~1320°C) makes the actions for the segregation reduction a challenging task, even for low-dilution processes. However, the more uniform distribution of temperature inside the groove with a rotating arc can minimize this issue. According to Guo *et al*. [7], the enhancement of arc rotation provokes the increase of temperature at the fusion line, thus improving the mixing ratio at the interface and reducing the supercooling degree of the transition zone. The high Ni content of the base metal also contributes to decreasing the liquidus temperature. The final result is a significant reduction of the segregation [7]. It explains the apparently controversial result obtained in this work, with solely austenite being predicted and observed in the transition zone. Figure 8–9 confirm that the GMAW-RE was effective in mitigating this issue since the narrow transition zone presented an austenitic microstructure solely. Some studies [12,34] have highlighted that steep chemical gradients in this region, caused by dilution between Ni-based filler metals and Fe-based 9% Ni steel, exert a strong effect on the local phase stability and transformation behavior. These results agree with other works [35], where the GMAW-RE process was successfully adopted to avoid the formation of deleterious microstructures, mainly in claddings, where this effect is more severe.

The novelty shown in this work for groove weldments corroborates a better performance of a 9% Ni narrow gap joint obtained by the GMAW-RE process.

2) HAZ properties equivalent to the base metal

In general, the 9% Ni steel exhibits a martensitic microstructure containing approximately 5% retained austenite due to the combination of high hardenability and Ni content [8]. However, the rotation of the electric arc modifies the joint temperature profile, which induces the formation of a mixed microstructure composed of tempered martensite and bainite due to the lower cooling rates [7]. In fact, while the arc energy is concentrated at the center of the bead in the conventional GMAW process, the wire rotation periodically directs the energy toward the groove walls [36–38], which imposes a welding thermal cycle with higher temperatures in the HAZ. As a consequence, the peak and period in high temperatures are higher for the same heat input applied, thus inducing longer cooling times. In addition, the segregation bands in the base metal (Figure 11) increase the heterogeneity of composition and also contribute to the formation of martensite and auto-tempered martensite due to the local segregation. The lower cooling rate promotes the formation of auto-tempered martensite, contributing to the stabilization of the internal energy state of the grains and limiting the plastic strain accumulation [39]. The microstructure composed of bainite, martensite, and auto-tempered martensite in the CGHAZ of 9% Ni steels has been obtained in various works [8,34,39–41].

Figure 14 and Table 4 show that the HAZ has mechanical properties equivalent to the base metal. Besides the ultimate tensile strength, the impact toughness of all positions studied showed values well above the minimum required for all industrial applications. It is an important result because the loss of impact toughness after welding is the main concern in the manufacturing of welded vessels, such as LNG tanks, for cryogenic environments [42]. Interestingly, the rotation of the electric arc was beneficial in the case of the 9% Ni steel, by decreasing the cooling rate of the HAZ and inducing the formation of auto-tempered martensite with a lower hardness and a high impact toughness. In this study, the results (Figure 14) were well above the minimum required for all positions studied, characterizing a suitable performance of the HAZ without deleterious effect on this property. It is also important to note that these results are higher than those obtained by conventional processes [5,8,12,14,25,28].

Figure 14 also reveals that the impact toughness of the HAZ close to the fusion line is higher than that of the base metal. Although it seems controversial since the latter position has a more refined microstructure compared with the HAZ (Figure 11 and Table 3), it is important to consider the negative influence of the banding. These segregation bands, widely observed in base metals [29], disrupt the homogeneity of the 9% Ni steel microstructure and contribute to reducing the impact toughness. Although the literature registers that the fraction of austenite is also important for impact toughness, it is noted that all positions show equivalent results.

5. Conclusions

The main conclusions are:

1) The 9% Ni steel narrow gap welded joint obtained by the GMAW-RE process showed suitable mechanical properties and absence of sidewall lack of fusion;

2) The rotation of the electric arc induced a mixed microstructure composed of tempered martensite and bainite at the HAZ;

3) The impact toughness of the HAZ was well above the required value for cryogenic structures;

4) The absence of martensite in the transition zone is an important novelty for quality welded joints and;

5) The 9% Ni steel welded by the GMAW-RE process using the Inconel as filler metal can become an advantageous alternative for LNG tanks.

Acknowledgements

The authors thank CEFET-RJ, UFRJ, Binzel, and White Martins for supporting this work.

References

[1] H. T. Serindag, and G. Çam, "Characterization of microstructure and properties of dissimilar AISI 316L/9Ni low-alloy cryogenic steel joints fabricated by gas tungsten arc welding," *Journal of Materials Engineering and Performance*, vol. 32, pp.7039–7049, 2023.

[2] S. Gook S,· A. El-Batahgy, A. Gumenyuk, M. Biegler, and M. Rethmeier, "Application of hybrid laser arc welding for construction of LNG tanks made of thick cryogenic 9% Ni steel plates," *Lasers Manufacturing and Materials Processing*, vol. 10, pp. 659–680, 2023.

[3] H. Zhu, X. Yang, K. Liu, X. Wang, Y. Du, and J. Zou, "Comparative studies on microstructure and toughness of 9%Ni steel joints welded by SMAW and GTAW," *Materials Technology*, vol. 58, pp. 477–484, 2024.

[4] A. Kern, U. Schriever, and J. Stumpfe, "Development of 9% nickel steel for LNG applications," *Steel Research International*, vol.78, pp.189–194, 2007.

[5] A. El-Batahgy, M. R. Elkousy, A. A. Al-Rahman, A. Gumenyuk, M. Rethmeier, and S. Gook, "Retaining mechanical properties of GMA-welded joints of 9%Ni steel using experimentally produced matching ferritic filler metal," *Materials*, vol. 15, no. 23, p. 8538, 2022.

[6] K. Yamasaki, H. Maniwa, Y. Kitagawa, T. Miwa, and K. Ishizaki, "Development of automatic welding system for 9% Ni steel LNG tanks," *Kobelco Technology Review*, vol.41, no. 3, pp. 36–42, 2024.

[7] W. Guo, Y. Cai, B. Wang, B. Zhang, and W. Mu, "Effects of axial magnetic field on Fe-Ni interface macrosegregation of 9%Ni steel welds filled with Ni-based alloy," *Journal of Materials Processing Technology*, vol. 315, p. 117889, 2023.

[8] J. Cheon, H. Jun, J. Kim, J. W. Kim, Y.-D. Kim, and C. Ji, "Effect of Ni-based filler metal types on microstructure and cryogenic impact toughness of FCAW welded 9 % nickel steel," *Journal of Materials Research and Technology*, vol. 39, pp. 4683–4695, 2025.

[9] K. Li, X. Wang, S.-S. Rui, X. Li, S. Li, Q. Sun, Y. Zhang, and Z. Cai, "Fatigue crack growth mechanism of Ni–based weld metal in a 9% Ni steel joint," *Materials Science and Engineering A*, vol. 832, p. 142485, 2022.

[10] X. Fan, Y. Li, Y. Qi, X. Cai, Z. Wang, and C. Ma, "Mechanical properties of cryogenic high manganese steel joints filled with nickel-based materials by SMAW and SAW," *Materials Letters*, vol. 304, p. 130596, 2021.

[11] Y. Qiangqiang, J. Chuanbao, C. Chonglong, W. Yinggand, H. Zhiwen, and Z. Qinye, "Rotating arc narrow gap vertical welding equipment for large 9% Ni steel storage tanks," *Electric Weld Machine*, vol. 54, no. 3, pp. 1–11, 2024.

[12] W. Mu, Y. Cai, M. Wang, and M. Hu, "Microstructure characteristics and properties of fusion boundary in 9%Ni steel joint filled with Ni-based alloy," *Materials Characterization*, vol. 165, p. 110390, 2020.

[13] M. Park, J. Kim, C. Pyo, J. Son, and J. Kim, "Research for the optimal flux-cored arc welding process of 9% nickel steel using multi object optimization with solidification crack susceptibility," *Materials*, vol. 14, no. 7, p. 1659, 2021.

[14] H. T. Serindağ, C. Tardu, I. O. Kirçiçek, and G. Çam, "A study on microstructural and mechanical properties of gas tungsten arc welded thick cryogenic 9% Ni alloy steel butt joint," *CIRP Journal of Manufacturing Science and Technology*, vol. 37, pp. 1–10, 2022.

[15] Y. Zhu, W. Mu, Y. Cai, D. Xin, and M. Wang, "A novel high-efficient welding technology with rotating arc assisted by laser and its application for cryogenic steels*," Journal of Manufacturing Processes*, vol. 68, pp. 1134–1146, 2021.

[16] C. P. Ferreira Jr, A. N. S. Alves, J. J. Carvalho, J. Casanova, and S. D. Brandi, "Caracterização mecânica e microestrutural da zona de transição do aço 9% Ni revestido com Inconel 625®," *Soldagem & Inspeção*, vol. 26, p. e2604, 2021.

[17] B. Wei, C. Jia, W. Wu, C. Fang, and C. Wu, "Stirring effect of the rotating arc on the molten pool during non-axisymmetric tungsten NG-GTAW," *Journal of Materials Processing Technology*, vol. 285, p. 116769, 2020.

[18] J. F. M. Costa, W. S. Filho, J. C. F. Jorge, M. C. Mendes, L. F. G. de Souza, T. de C. Chuvas, and L. S. Araujo, "Investigation on the ASTM A516 Grade 70 narrow gap welded joints obtained by the GMAW process with rotating electrode," *International Journal of Advanced Manufacturing Technology*, vol. 134, no. 7–8, pp. 3453–3464, 2024.

[19] G. M. S. Silveira, J. C. F. Jorge, L. F. G. de Souza, M. C. Mendes, F. A. C. Almeida, W. A. S. Filho, J. F. M. Costa, and T. C. Chuvas, "Microstructural characterization and mechanical properties of high‐strength steel weld metals obtained by GMAW process with rotating electrode (GMAW‐RE)," *Journal of Brazilian Society Mechanical Science Engineering*, vol. 43, Art. no. 221, 2021.

[20] G. Arunkumar, M. Umar, and P. Sathiya, "Experimental investigation and characterization analysis of super austenitic stainless steel using spin arc-gas metal arc welding process," *Welding in the World*, 2025.

[21] N. Sankar, S. Malarvizhi, and V. Balasubramanian, "Performance and characteristics of stationary arc and rotating arc-gas metal arc welded DMR 249 naval grade steel joints," *Materials Performance Characterization*, vol. 11, p. 170–192, 2022.

[22] G. Z. Batista, V. Trindade, M. C. Mendes, L. F. G. de Souza, and J. C. F. Jorge, "Effect of GMAW rotating electrode frequency variation on the X80 seamless pipe mechanical properties and microstructure," *International Journal of Advanced Manufacturing Technology*, vol. 141, pp. 1935–1947, 2025.

[23] *Standard Test Methods for Tension Testing of Metallic Materials*, ASTM E8M-04, West Conshohocken, 2010.

[24] G. Batista, V. B. Trindade, M. C. Mendes, L. F. G. de Souza, and J. C. F. Jorge, "Microstructure characterization of the coarse grain heat affected zone of X80 steel welded by the GMAW-RE process," *Metallography, Microstructure and Analysis*, vol. 14, no. 1, pp. 355–368, 2025.

[25] A. F. M. Khourshid, and M. A. Ghanem, "The influence of welding parameters on brittle fracture of liquefied natural gas storage tank welded joint," *Materials Science Applied*, vol. 34, pp. 198–204, 2013.

[26] T. Wingens, "Retained austenite benefits or avoidance requires dependable determination," *Heat Treat; Proceeding of the 31st ASM Heat Treating Society Conference*, pp. 14–16, 2021.

[27] S. Pashangeh, H. R. K. Zarchi, S. S. G. Banadkouki, and M. C. Somani, "Detection and estimation of retained austenite in a high strength Si-bearing bainite-martensite-retained austenite micro-composite steel after quenching and bainitic holding (Q&B), *Metals*, vol. 9, no. 5, p. 492, 2019.

[28] W. Guo, Y. Cai, B. Wang, W. Mu, and D. Xin, "Effect of microstructure synergism on cryogenic toughness for CGHAZ of low-carbon martensitic steel containing nickel," *Materials Science and Engineering A*, vol. 830, p. 142240, 2022.

[29] A. V. Passos, J. C. Payão Filho, V. H. P. M. Oliveira, M. C. G. Rios, and F. W. C. Farias, "Effect of multiple welding thermal cycles on microstructure and stress corrosion crack susceptibility of the 9 % Ni steel," *Engineering Failure Analysis*, vol. 180, p. 109858, 2021.

[30] *Standard Specification for pressure vessel, plates, alloy steel, quenched and tempered 8 and 9% Nickel*, ASTM A 553/553M-17, West Conshohocken, USA, 2019.

[31] P. H. G. Dornelas, J. C. P. Filho, V. H. P. M. Oliveira, D. de O. Moraes, and P. Z. Junior., "Effect of the interpass temperature on simulated heat-affected zone of gas metal arc welded API 5L X70 pipe joint," *International Journal of Advanced Manufacturing Technology*, vol. 119, pp. 261–274, 2022.

[32] F. W. C. Farias, J. C. P. Filho, D. A. S. Júnior, R. N. de Moura, and M. C. G. Rios, "Microstructural characterization of Ni-based superalloy 625 clad welded ona 9% Ni steel pipe by plasma powder transferred arc," *Surface and Coatings Technology*, vol. 374, pp. 1024–1037, 2019.

[33] C. P. Alvarães, F. C. A. Madalena, L. F. G. Souza, J. C. F. Jorge, L. S. Araujo, and M. C. Mendes, "Performance of the Inconel 625 weld overlay obtained by FCAW process,"*Materia*, vol. 24, pp. 1–12, 2019.

[34] J. Y. Hwang, K. Choi, and H. Y Jung, "Correlation between microstructure and mechanical properties of welding joint in 9% Ni steel with two types of Ni-based superalloy filler metals," *International Journal of Advanced Manufacturing Technology*, vol. 22, pp. 2761–2773, 2022.

[35] J. F. M. Costa, P .L. Lacerda, H. A. Y. Magalhães, J. C. F. Jorge, L. F. G. de Souza, M. C. Mendes, L. S. Araujo, and H. N. Farneze, "Inconel 625 weld claddings obtained by the GMAW-RE with rotating electrode," *International Journal of Advanced Manufacturing Technology*, vol. 132, no. 11–12, pp. 5647–5661, 2024.

[36] J. Y. Wang, Y. S. Ren, F. Yang, and H. B. Guo, "Novel rotation arc system for narrow gap MAG welding" *Science Technology of Welding and Joining*, vol. 12, no. 6, pp. 505–507, 2007.

[37] Q. Bai, N. Guo, Y. F. Han, J. Zhang, and M. R. Wang, "Analysis of temperature distribution in rotating arc welding," *Advanced Materials Research*, vol. 472–475, pp. 1346–1352, 2012.

[38] G. Z. Batista, V. Trindade, M. C. Mendes, L. F. G. de Souza, and J. C. F. Jorge, "Microstructure characterization of the coarse grain heat affected zone of X80 steel welded by the GMAW-RE process," *Metallography, Microstructure, and Analysis*, vol. 14, no. 2, pp. 355–368, 2025.

[39] J. M. Zhang, H. Li, F. Yang, Q. Chi, L. K. Ji, and Y. R. Feng, "Effect of heat treatment process on mechanical properties and microstructure of a 9% Ni steel for large LNG storage tanks," *Journal of Materials Engineering and Performance*, vol. 22, pp. 3867–3871, 2013.

[40] M. C. G. Rios, J. C. P. Filho, F. W. C. Farias, A. V. Passos, and V. H. P. M. e Oliveira, "Microstructural characterization of the physical simulated and welded heat-affected zone of 9% Ni steel pipe," *Journal of Materials Research and Technology*, vol. 17, pp. 3033–3046, 2022.

[41] R. W. Fonda, and G. Spanos, "Effects of cooling rate on transformations in a Fe-9 pct Ni steel" *Metallurgical and Materials Transactions A*, vol. 45, pp. 5982–5995, 2014.

[42] T. Xu, Y. Shi, Z. Jiang, B. Liu, J. Zhan, and Z. Wang, "An extraordinary improvement in cryogenic toughness of K-TIG welded 9Ni steel joint assisted by alternating axial magnetic field," *Journal of Materials Research and Technology*, vol. 25, pp. 3071–3077, 2023.